One-pot synthesis of $BaMg_{1/3}Ta_{2/3}O_{3-x}N_y$/$Ta_3N_5$ heterostructures as H_2-evolving photocatalysts for construction of visible-light-driven Z-scheme overall water splitting

Junyan Cui[a,b], Yu Qi[b], Beibei Dong[b], Linchao Mu[b], Qian Ding[b], Gang Liu[a], Mingjun Jia[a], Fuxiang Zhang[b,*], Can Li[b,*]

[a] Key Laboratory of Surface and Interface Chemistry of Jilin Province, College of Chemistry, Jilin University, Changchun 130012, China
[b] State Key Laboratory of Catalysis, Collaborative Innovation Center of Chemistry for Energy Materials (iChEM), Dalian Institute of Chemical Physics, Chinese Academy of Sciences, Dalian National Laboratory for Clean Energy, Dalian, 116023, China

ARTICLE INFO

ABSTRACT

Nitrogen-doped oxides are one kind of photocatalysts with wide spectrum absorption for promising solar water splitting, but they usually exhibit poor charge separation and thermal instability in air, leading to challenging construction of overall water splitting (OWS) system. Here we adopt one-pot nitridation strategy to synthesize a series of heterostructured photocatalysts based on Ta_3N_5 and the newly reported nitrogen-doped oxide $BaMg_{1/3}Ta_{2/3}O_{3-x}N_y$ (denoted as BMTON) with absorption wavelength of 560 nm. The as-obtained typical heterostructure $BaMg_{1/3}Ta_{2/3}O_{3-x}N_y$/$Ta_3N_5$ (denoted as $BMTON/Ta_3N_5$) is found to exhibit superior charge separation and transfer ability with respect to the corresponding counterparts, as has been ascribed to their well-matched band gap structure and intimate interface contact. As a result, the photocatalytic activity of proton reduction over the optimized heterostructure $BMTON/Ta_3N_5(0.4)$ is about 20 times higher than that of the counterparts, based on which effective Z-scheme OWS system under visible light irradiation can be realized by using the heterostructure $BMTON/Ta_3N_5$ as H_2-evolving photocatalyst. This work not only gives a further proof that one-pot nitridation is a general strategy to fabricate heterostructure composed of nitrogen-doped complex oxide for enhanced charge separation and photocatalytic performance, but also demonstrates the promising future of nitrogen-doped oxide in constructing artificial photosynthesis devices.

1. Introduction

Photocatalytic overall water splitting (OWS) for H_2 production is regarded as a "green" technology to alleviate the energy crisis [1–4]. To efficiently utilize the visible region ($\lambda \geq 400$ nm) which occupies the main part of solar spectrum, the development of visible-light-driven photocatalysts is one of the most promising ways [5–9]. Various strategies have been developed for extended visible light utilization, among which nitrogen incorporation into oxide is one of the most effective approaches [10,11]. However, the nitrogen-doped oxides not only generally confront poor charge separation ability, but also suffer from thermal instability in air, as greatly constraining their structure adjustment and surface modification for promotion of charge separation as well as performance enhancement. Consequently, the nitrogen-doped oxide photocatalysts have been mostly reported for H_2-evolving or O_2-evolving half reaction, while few of them were reported for

assembly of effective OWS systems [12–15]. In the view point of solar-to-chemical energy conversion, the assembly of OWS with positive Gibbs free energy changes instead of half reactions is requisite [16]. Accordingly, it is still desirable to construct OWS system by using nitrogen-doped oxide photocatalysts.

Recently we have reported a novel nitrogen-doped complex perovskite oxide $BaMg_{1/3}Ta_{2/3}O_{3-x}N_y$ (denoted as BMTON) that was demonstrated to be active for both proton reduction and water oxidation half reactions under visible light irradiation [17]. However, it was infeasible for OWS regardless of one-step or two-step (also called Z-scheme) system, even though its band structures are satisfied with the requirement of thermodynamics for both water reduction and oxidation. The main problem has been proposed to lie in its poor charge separation ability, leading to ineffective reaction kinetics of water splitting. To address its low reaction activities of half reactions, continuous efforts on promotion of charge separation are desirable.

Different from most of oxide photocatalysts, the nitrogen-doped oxide BMTON suffers from poor thermal stability in air or inert gases. As a consequence, most previous strategies for promotion of charge separation on oxides become unsuitable and infeasible [18–20]. To overcome the shortcoming of poor thermal stability in air, recently we have developed one-pot nitridation strategy to fabricate heterostructures of $MgTa_2O_{6-x}N_y/TaON$ and $BaTaO_2N/Ta_3N_5$ to promote the charge separation efficiency as well as photocatalytic performances [21,22]. The advantages of one-pot nitridation strategy are known to not only efficiently avoid the thermal treatment in air, but also be favorable for creating intimate hetero-interface for enhanced charge separation due to the high temperature process adopted under the flow of ammonia.

Encouraged by our previous successful construction of $MgTa_2O_{6-x}N_y/TaON$ and $BaTaO_2N/Ta_3N_5$ heterostructures, here we further introduce the one-pot nitridation preparation of $BaMg_{1/3}Ta_{2/3}O_{3-x}N_y/Ta_3N_5$ (denoted as $BMTON/Ta_3N_5$) heterostructures by employing mixtures of complex perovskite oxide $BaMg_{1/3}Ta_{2/3}O_3$ (BMTO) and Ta_2O_5 as precursors under the flow of ammonia at 1223 K for 12 h. The oxide precursors were prepared by a modified citric acid method [23] and the molar ratios of Mg/Ta were adjusted for preparation of a series of samples. The successful formation of heterostructure between BMTON and Ta_3N_5 is mainly ascribed to their similar structure properties and synthesis conditions [17,24]. Different from previous one-pot fabrication of heterostructures, it should be the first construction of heterostructure containing quinary structure BMTON, demonstrating the generality of the one-pot nitridation approach in fabricating nitrogen-doped oxide based heterostructured samples. Based on the HRTEM images and time-resolved infrared spectra, the highly intense interface contact and prolonged photoexcited carrier lifetime well confirmed the enhanced photo-generated charge separation and transfer ability. Under optimal conditions, the H_2-evolving half reaction activity can be promoted by about twenty times, and visible-light-driven Z-scheme OWS can be finally achieved on the basis of our recently developed nitrogen-doped oxide BMTON as the H_2-evolving photocatalyst.

2. Experimental

2.1. Materials and reagents

For the preparation of $BMTON/Ta_3N_5$ samples, $TaCl_5$ (99.99%, Alfa Aesar), Ta_2O_5 (99.99%, Alfa Aesar), $Mg(NO_3)_2$ (99.5%, Sinopharm Chemical), $Ba(NO_3)_2$ (99.5%, Sinopharm Chemical), anhydrous citric acid (99.5%, Sinopharm Chemical) and CH_3OH (99.5%, Sinopharm Chemical) were used. WO_3 (99.99%, High Purity Chemical) was used as the water oxidation photocatalyst, $H_2PtCl_6 \cdot 6H_2O$ (99.5%, Sinopharm Chemical) was employed to deposit Pt and PtO_x cocatalysts, respectively. CH_3OH (99.5%, Sinopharm Chemical) and NaI (99.5%, Guangfu Chemical) were used as the sacrificial electron donors. La_2O_3 (99.95%, Sinopharm Chemical) was applied as a buffer agent. All chemicals were used as-purchased without further purification.

2.2. Preparation of $BMTON/Ta_3N_5(n)$ samples

The oxide precursors of the heterostructures were prepared by a modified citric acid method [23]. Typically, 2 mmol of $TaCl_5$ was dissolved in 40 mL of methanol, and 10 mmol of anhydrous citric acid (CA) was added, followed by addition of stoichiometric $Mg(NO_3)_2$, $Ba(NO_3)_2$. Then, 40 mL of H_2O was added, the reaction mixture was mechanically stirred until it became transparent. A certain amount of bulk Ta_2O_5 was subsequently added to above solution, and continuously stirred for one hour. The resulting solution was heated at 493 K to evaporate the liquid. And the powder obtained was subsequently calcined at 1073 K for 2 h in air. The final product was well-crystalline oxide powder. Finally, the heterostructured samples were prepared by a thermal nitridation method. Typically, 0.5 g oxide sample was nitrided under ammonia flow (250 ml min^{-1}) at 1223 K for 12 h. After naturally cooling to room temperature, the sample was collected and stored in a desiccator for use. The as-obtained heterostructured samples $BaMg_{1/3}Ta_{2/3}O_{3-x}N_y/Ta_3N_5$ are correspondingly denoted as $BMTON/Ta_3N_5(n)$, where the molar ratio of Ba/Mg was a fixed constant of 3.0 according to the stoichiometric ratio of BMTON and "n" stands for the adjustable molar ratios of Mg/Ta (n = 0, 0.1, 0.2, 0.3, 0.4, 0.45, 0.5). For comparison, single phase BMTON (n = 0.5) was prepared without adding Ta_2O_5, while Ta_3N_5 (n = 0) was synthesized by nitriding corresponding oxide Ta_2O_5. Besides, the physically mixed sample of the optimal heterostructure was prepared by a facile physical grinding process, which is denoted as $BMTON/Ta_3N_5(0.4)$-mix.

2.3. Deposition of Pt or PtO_x cocatalyst

The 0.5 wt% Pt cocatalyst was deposited by conventional impregnation and subsequent H_2 reduction. Typically, 0.2 g sample was immersed in ca. 2 mL H_2PtCl_6 aqueous solution, and sonicated for ca. 5 min. After the solution was completely evaporated in a water bath at 353 K, the resulting powder was collected and reduced at 473 K for 1 h under a flow of 5 vol% H_2/Ar (200 ml min^{-1}). For the O_2-evolving photocatalyst of Z-scheme system, PtO_x was deposited on the surface of WO_3 in air. Typically, 0.3 g WO_3 was annealed at 773 K for 2 h, and then 0.2 g annealed sample was immersed in a calculated amount of H_2PtCl_6 aqueous solution with sonicating for ca. 5 min. After complete evaporation in a water bath at 353 K, the resulting powder was collected and annealed in air at 798 K for 0.5 h.

2.4. Characterizations of photocatalysts

X-ray diffraction (XRD) measurement was carried out on a Rigaku D/Max-2500/PC powder diffractometer (Cu Kα radiation) with operating voltage of 40 kV and operating current of 200 mA. The scan rate of 5° min^{-1} or 0.5° min^{-1} was applied at a step size of 0.02°. UV-Vis diffuse reflectance spectra (DRS) were recorded on a UV-Vis spectrophotometer (JASCO V-550) equipped with an integrating sphere, and $BaSO_4$ powder was used as the reference for baseline correction. The morphologies and particle sizes were examined by a high-resolution scanning electron microscopy (HRSEM; S-5500, Hitachi). High-resolution transmission electron microscopy (HRTEM) images were obtained on Tecnai G2 F30 S-Twin (FEI Company) with an accelerating voltage of 300 kV. The Brunauer-Emmett-Teller (BET) surface area was measured at 77 K using a Micromeritics ASAP 2000 adsorption analyzer. X-ray photoelectron spectroscopy (XPS, Thermo Esclab 250Xi, a monochromatic Al Kα X-ray source) was carried out to check the binding energies of elements and judge the relative positions of valence bands, and the C 1 s peak (284.6 eV) was employed for reference. The transient IR absorption signals were recorded on the Nicolet 870 FTIR spectrometer with the MCT detector. The pulse laser of 355 nm (1 Hz, 3 mJ/pulse) was used to excite the samples.

2.5. Photocatalytic reactions

The photocatalytic reactions were carried out in a Pyrex top-irradiation-type reaction vessel connected to a closed gas circulation system.

The reaction mixture was evacuated to ensure complete air removal, and then irradiated from the top side with a 300 W xenon lamp using a filtration mirror which was equipped with an optical filter (Hoya, L-42; $\lambda \geq 420$ nm) to cut off the light in the ultraviolet region. A flow of cooling water was used to maintain the reaction suspension at room temperature. The evolved gases were analyzed by gas chromatography (Agilent; GC-7890 A, MS-5 A column, TCD, Ar carrier). The pH value before and after the photocatalytic overall water splitting reaction is similarly kept to be ca. 6.

2.6. Measurement of apparent quantum efficiency (AQE)

The AQE measurement was carried out using a Pyrex top-irradiation-type reaction vessel and a 300 W xenon lamp fitted with band-pass filters. The number of photons reaching the reaction solution was measured using a calibrated Si photodiode (LS-100, EKO Instruments Co., LTD.), and the AQE (φ) was calculated according to the following equation:

$$\varphi\ (\%) = (AR\ /\ I) \times 100$$

where A represents a coefficient (4 for H_2 evolution; 8 for O_2 evolution in the Z-scheme system), R represents the evolution rate of H_2 or O_2 in the initial one hour irradiation and I represents the absorption rate of incident photons, respectively. It was assumed that all incident photons were absorbed by the suspension. The total number of incident photons at the wavelength of 420 nm was measured to be 2.55×10^{20} photons h^{-1}."

2.7. Electrode preparation and photoelectrochemical measurements

For the Mott-Schottky (M–S) measurement, the samples were deposited on FTO conducting glass by the electrophoretic deposition (EPD). Typically, the EPD was carried out in an acetone solution (50 mL) containing powder sample (50 mg) and iodine (20 mg), which was dispersed by sonication for 20 min. The FTO electrode was immersed in above solution, paralleling with another FTO electrode, and the distance between these two electrodes was 1 cm. 20 V was applied for 1 min using a potentiostat (ITECH IT6834), then the prepared electrodes were calcined in NH_3 at 723 K for 1 h. The M–S measurement was carried out on a Princeton Applied Research PARSTAT 2273, using 0.1 M Na_2SO_4 aqueous solution as electrolyte with pH value of 8.5 adjusted by NaOH. The frequency and amplitude of AC potential were 1 kHz and 0.01 V, respectively. The electrochemical impedance spectroscopy (EIS) measurement was conducted in 0.1 M NaI + 0.1 M Na_2SO_4 aqueous solution with pH value of 9.0, and an AM 1.5 G was served as the light source.

All the (photo) electrochemical tests were conducted in a 3-electrode system with a quartz window. A piece of platinum foil was used as counter electrode and saturated calomel electrode (SCE, 0.241 V vs RHE) as the reference electrode. The potential was transferred to the reversible hydrogen electrode (RHE) scale by Nernst equation as below:

$$E\ (RHE) = E\ (SCE) + 0.059 * pH + 0.241$$

3. Results and discussion

Fig. 1a gives the XRD patterns of typical samples with different n (0-0.5) values, based on which all of the diffraction peaks are sharp and intense, showing their highly crystalline features. As for the sample with n value of 0.5, all the diffraction peaks can be indexed to the cubic perovskite BMTO (PDF # 87–1733), indicating that nitrogen-doped sample BMTON can well maintain the crystalline structure of precursor oxide BMTO [25]. Similarly, single phase of Ta_3N_5 can be indexed for the sample with n value of 0. Comparatively, diffraction peaks of the samples with n values located between 0 and 0.5 can be indexed as the integration of BMTON and Ta_3N_5 compounds, and intensities of peaks assigned to Ta_3N_5 decrease with the increasing molar ratio of Mg/Ta (n value). Furthermore, with decreasing the molar ratio of Mg/Ta, the diffraction peaks of the heterostructures in the diffraction angle region of 30–32° are slightly shifted to smaller angles compared to the single phase BMTON, indicating that some oxygen atoms should have been substituted by nitrogen atoms with a little bigger ionic radius (N^{3-}: 0.132 nm; O^{2-}: 0.124 nm). This result well demonstrates the increasing amount of doped nitrogen atoms and possible formation of heterostructures.

Fig. 1b gives the UV-Vis diffuse reflectance spectra (DRS) of typical samples with n values of 0-0.5, in which all of them exhibit wide visible light absorption. As similar to our previous observation, the absorption edge of BMTON is about 560 nm [17]. However, with decreasing molar ratio of Mg/Ta, the absorption edges of the heterostructures are continuously red-shifted until the formation of single phase of Ta_3N_5 showing absorption edge of ca. 600 nm. Besides the change of absorption edge, the absorption background of the heterostructured samples originating from reduced tantalum species (e.g. Ta^{4+}, Ta^{3+}) [26,27] decreases with the increasing molar ratio of Mg/Ta. The results are totally different from the single counterparts where the BMTON shows the lowest background absorption while Ta_3N_5 displays the largest. It means that a strong interaction between BMTON and Ta_3N_5 happens during the synthesis process, further demonstrating the formation of the heterostructures. As an extended discussion, we also compare the UV-Vis DRS of BMTON/Ta_3N_5(0.4) sample with the physically mixed sample of BMTON and Ta_3N_5 (denoted as BMTON/Ta_3N_5(0.4)-mix) using the single counterparts as references. As seen in the insert of Fig. 1b, similar absorption backgrounds are observed for the BMTON/Ta_3N_5(0.4) and BMTON/Ta_3N_5(0.4)-mix samples, both of which are located between the single phases of BMTON and Ta_3N_5. However, the absorption edge of the BMTON/Ta_3N_5(0.4) is obviously blue-shifted compared to that of BMTON/Ta_3N_5(0.4)-mix, indirectly verifying the formation of heterostructure as well as strong interaction between BMTON and Ta_3N_5.
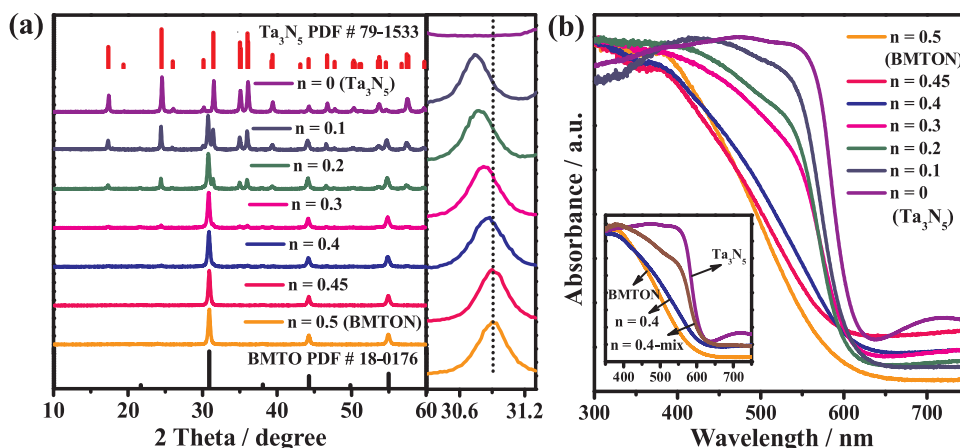

Fig. 1. Structural characterizations of as-obtained BMTON/Ta_3N_5(n) (n = 0-0.5) samples (n stands for the molar ratio of Mg/Ta): (a) XRD and enlarged XRD patterns; (b) UV-Vis diffuse reflectance spectra.
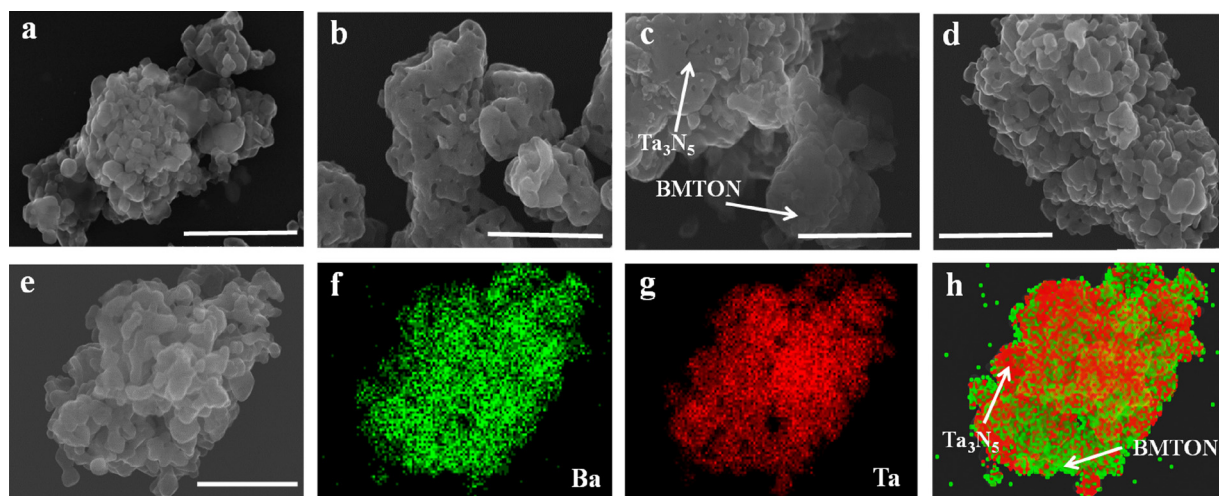
Fig. 2. The HRSEM images of typical samples: (a) BMTON, (b) Ta_3N_5, (c) BMTON/Ta_3N_5(0.4)-mix, (d) BMTON/Ta_3N_5(0.4); and the EDS elemental mappings of the heterostructured sample BMTON/Ta_3N_5(0.4): (e) HRSEM image, (f) Ba element, (g) Ta element, (h) simulated dispersion of BMTON and Ta_3N_5, scale bar = 500 nm.

The formation of heterostructures can be further confirmed by the HRSEM images and their elemental mapping results. As seen in Fig. 2, the single phase of Ta_3N_5 (n = 0) is porous with the particle size of 300–500 nm (Fig. 2b), while the single phase BMTON (n = 0.5) is smooth with the particle size of 30–50 nm (Fig. 2a). The two phases can be easily distinguished from the HRSEM image of typical BMTON/Ta_3N_5(0.4)-mix sample due to their remarkable difference in morphology (Fig. 2c). Comparatively, the morphology of BMTON/Ta_3N_5(0.4) sample emerges as a dense aggregate with uniform nanoparticles of 50–80 nm (Fig. 2d), which is totally different from the above mentioned samples. As a result of strong interaction and formation of heterostructure, the phases of BMTON and Ta_3N_5 cannot be easily distinguished from each other. Alternatively, energy-dispersive spectroscopy (EDS) mapping analysis of the sample BMTON/Ta_3N_5(0.4) was carried out to further reveal the formation of heterostructures. As seen in Fig. 2e-g, the Ta element originating from both BMTON and Ta_3N_5 is dispersed everywhere, while the Ba element just contained in BMTON phase is only dispersed in some specific places. This can be easily understood that the places with Ba element mapping dominantly stand for the existence of BMTON, while the locations with Ta element mapping but shortage of Ba element mapping stand for the Ta_3N_5 species. On the basis of this, we can reasonably make a simulation on the heterostructured sample BMTON/Ta_3N_5(0.4) (Fig. 2h).

To give a direct observation on the formation of heterostructure, the TEM and HRTEM measurements on the typical sample were carried out.

Fig. 3a gives the typical TEM image of BMTON/Ta_3N_5(0.4) sample, from which the decreasing particle size of 50–80 nm can be further verified. Fig. 3b gives the representative HRTEM image, in which the interface of the heterostructure can be clearly observed. The clear lattice fringes reveal that the sample synthesized here is well crystallized, in a good accordance with above XRD patterns. On the basis of measurement of lattice distance, both phases of BMTON and Ta_3N_5 can be judged. Interestingly, the interfacial contact between BMTON and Ta_3N_5 is intimate, verifying the formation of heterostructure. The construction of heterostructure may result from their similar Ta-based octahedron units and the one-pot nitridation route with high temperature.

The relative band positions of BMTON and Ta_3N_5 are analyzed by combing their Mott-Schottky (M-S) plots and the UV-Vis DRS results. The bandgap of BMTON and Ta_3N_5 can be estimated to be 2.21 eV and 2.10 eV from the Kubelka-Munk function versus the energy of the light absorbed, respectively. In Fig. 4a, the flat band potentials of BMTON and Ta_3N_5 can be evaluated to be ca. -0.42 V and 0.05 V vs. RHE, respectively. The flat band potential of the typical BMTON/Ta_3N_5(0.4) sample was also measured to be located between them. In consideration of the fact that the bottom of the conduction band of one n-type semiconductor is commonly more negative by ca. 0.1-0.3 eV than the flat band potential [28], the conduction band positions of the n-type BMTON and Ta_3N_5 are estimated to be -0.62 V and -0.15 V, respectively. On the basis of above analysis, the relative band positions of
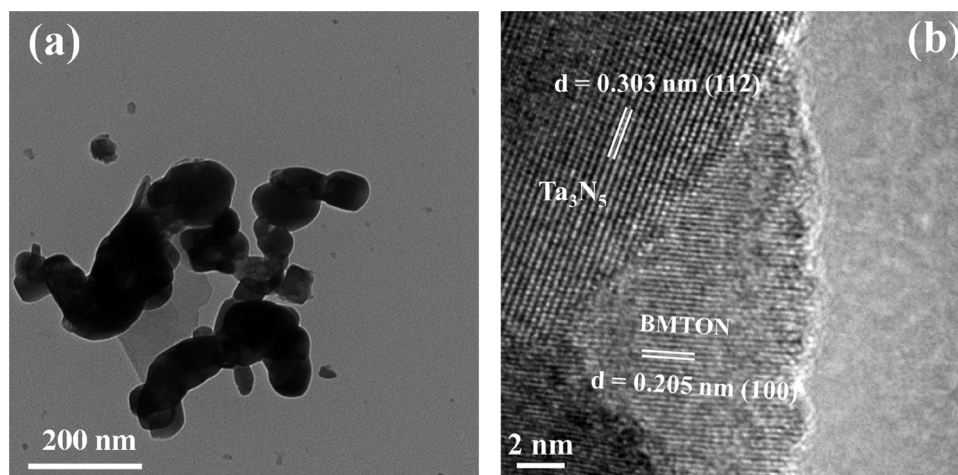

Fig. 3. Representative TEM (a) and HRTEM (b) images of the typical heterostructured sample BMTON/Ta_3N_5(0.4).
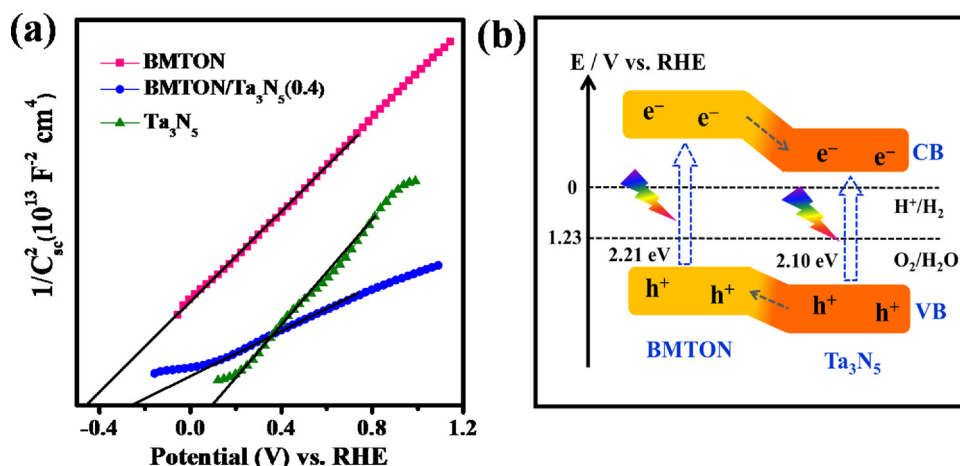
Fig. 4. Band gap characterizations of the typical samples: (a) Mott-Schottky plots of the typical sample electrodes. Electrolyte: 0.1 M Na_2SO_4 solution (pH = 8.5, adjusted by NaOH). Frequency: 1000 Hz; (b) Relative band positions of BMTON and Ta_3N_5 samples.

BMTON and Ta_3N_5 are deduced and shown in Fig. 4b, where the excited electrons of the heterostructured samples are expected to transfer from the conduction band of BMTON to that of Ta_3N_5, while the excited holes will transfer oppositely from Ta_3N_5 to BMTON. As a result of spatial separation of excited electrons and holes, the separation ability of photogenerated carriers will be promoted.

The photocatalytic H_2 evolution rates of the as-obtained series of samples were examined using the deposited platinum nanoparticles as the reduction cocatalyst in the presence of methanol under visible light irradiation ($\lambda \geq 420$ nm). No reaction occurs in the dark, and H_2 evolution can be only observed after light irradiation. As given in Fig. S1, the rate of H_2 evolution as a function of Mg/Ta ratio undergoes first increasing and subsequent decreasing. The optimized molar ratio of Mg/Ta is 0.4, whose H_2 evolution rate (22.9 μmol h^{-1}) is about 20 times higher than that of single BMTON (0.9 μmol h^{-1}) or Ta_3N_5 (1.3 μmol h^{-1}) photocatalyst. And it is also more superior to that of the BMTON/Ta_3N_5(0.4)-mix sample (2.2 μmol h^{-1}). It should be pointed out that only trace amount of N_2 (less than 0.5 μmol) was detected at the initial stage of reaction. In addition, all four typical samples show similar binding energy of Pt element (Fig. S2) [29], demonstrating that the cocatalyst Pt is not the essential factor affecting the photocatalytic water splitting performance. Therefore, the promoted photocatalytic activities should ascribe to the formation of heterostructure with intimate interface contact favoring the spatial charge separation. The dependence of the H_2 evolution rate on the BMTON/Ta_3N_5(0.4) sample as a function of irradiation wavelength is in a good accordance with its

UV-Vis diffuse reflectance spectra (Fig. 5a), indicating the H_2-evolving reaction is driven by the incident light absorbed. In addition, the corresponding plots of apparent quantum efficiency (AQE) vs. wavelength (λ) are also added in Fig. S3, the similar tendency to the UV-Vis DRS further indicates that the water splitting reaction is driven by photocatalysis.

To achieve efficient solar energy conversion, the assembly of OWS with positive Gibbs free energy changes is highly desirable. Normally, IO_3^-/I^- redox reagent is widely used as the redox electron mediator for construction of Z-scheme OWS system [16]. Here, the half reaction activities of the typical samples using NaI as the sacrificial reagent were first examined. As shown in Table S1, bare Ta_3N_5 has no H_2-evolution activity (0 μmol h^{-1}), and BMTON shows tiny H_2-evolution activity (0.28 μmol h^{-1}) in the NaI solution. With respect to the single phase of BMTON or Ta_3N_5, the physically mixed sample BMTON/Ta_3N_5(0.4)-mix exhibits slightly increased H_2 evolution activity (0.39 μmol h^{-1}), while the H_2 evolution activity (1.74 μmol h^{-1}) of the optimal heterostructure sample BMTON/Ta_3N_5(0.4) is greatly promoted. Obviously, the heterostructured sample could be well functioned as H_2-evolving photocatalyst in the Z-scheme system containing I^- ions.

In consideration of the PtO_x-WO_3 was extensively applied in the Z-scheme systems containing IO_3^-/I^- shuttle ions [30–32], we thus attempt to construct the Z-scheme OWS system by employing the heterostructured sample as the H_2-evolving photocatalyst, accompanying with PtO_x-WO_3 as the O_2-evolving photocatalyst, and IO_3^-/I^- as the redox electron mediator. As given in Fig. 5b, using Pt-Ta_3N_5 as the H_2-
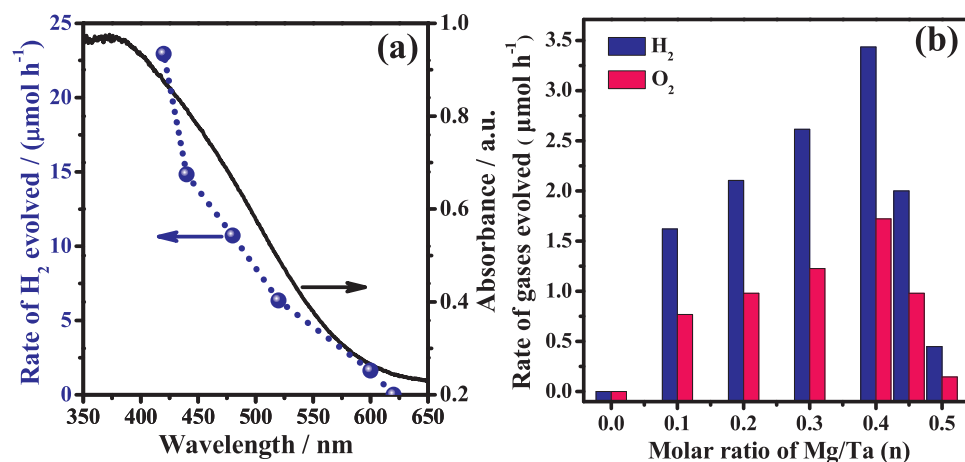

Fig. 5. (a) The dependence of photocatalytic H_2 evolution rate on the irradiation wavelength over the optimal BMTON/Ta_3N_5(0.4) sample[a]. The solid lines represent UV-Vis DRS of the heterostructure BMTON/Ta_3N_5(0.4). (b) Comparison of photocatalytic Z-scheme OWS performances using heterostructured photocatalysts with different molar ratios of Mg/Ta (n = 0.5 stands for BMTON; n = 0 stands for Ta_3N_5) as the H_2-evolving photocatalyst[b].
[a]Reaction conditions: 0.15 g 0.5 wt% Pt-BMTON/Ta_3N_5(0.4), 0.15 g La_2O_3, aqueous methanol solution (150 mL, 20 vol%), Pyrex top-irradiation type, 300 W xenon lamp ($\lambda \geq 420$ nm), 1 h irradiation.
[b]Reaction conditions: 50 mg 0.5 wt% Pt-BMTON/Ta_3N_5(n) (n = 0-0.5), 100 mg 0.45 wt% PtO_x-WO_3, 100 ml aqueous NaI solution (0.8 mM), Pyrex top-irradiation type, 300 W xenon lamp ($\lambda \geq 420$ nm), 1 h irradiation.

evolving photocatalyst, no obvious H_2 can be detected, indicating the infeasibility of Ta_3N_5 itself to drive the Z-scheme OWS. When using Pt-BMTON as the H_2-evolving photocatalyst, both H_2 and O_2 can be detected but the ratio of H_2/O_2 is not stoichiometric 2.0, demonstrating its similar ineffectiveness. Different from the single phase of BMTON or Ta_3N_5, the heterostructured samples used as the H_2-evolving photocatalysts can well drive the Z-scheme OWS to produce stoichiometric H_2 and O_2, among which the system with Pt-BMTON/Ta_3N_5(0.4) employed exhibits the optimal overall water splitting performance (H_2: 3.4 μmol h^{-1}, O_2: 1.7 μmol h^{-1}). The AQE was measured to be 0.1% at 420 nm by using the optimal Pt-BMTON/Ta_3N_5(0.4) sample as the H_2-evolving photocatalyst. It is interesting to note that the activity trend of Z-scheme OWS is similar to that of H_2-evolving half reaction (Fig. S1), proving that the evolution rate of H_2 may be the rate-determining step of the Z-scheme OWS system. As a reference, the stoichiometric H_2 and O_2 evolution were also observed when using the physically mixed sample Pt-BMTON/Ta_3N_5(0.4)-mix as H_2 evolution photocatalyst although the photocatalytic performance is poor (Table S1). It means that the charge transfer and photocatalytic performance promotion happen due to mechanical collision between BMTON and Ta_3N_5, further demonstrating thermodynamic feasibility of charge transfer between them. In addition, the multiple cycles of time course curves about the Z-scheme OWS based on the Pt-BMTON/Ta_3N_5(0.4) sample are shown in Fig. 6. The rates of H_2 and O_2 evolution slightly decreased with time, indicating that some undesirable reactions occurred during water splitting process. One is the competing reaction originating from the shuttle ions such as the reduction of IO_3^- and oxidation of I^-. The other is the back reaction of the evolved H_2 and O_2. It should be noted that this is a normal case and extensively observed in previous Z-scheme systems [31–35]. In addition, no obvious changes in the XRD patterns of the heterostructure BMTON/Ta_3N_5(0.4) before and after photocatalytic water splitting reactions demonstrate the photocatalysts are stable for water splitting in the experimental region (Fig. S5).

In this work, both BMTON and the heterostructured sample BMTON/Ta_3N_5(0.4) exhibit similar adsorptivities of I^- ions, thus the effect originating from the I^- ions absorptivity can be ignored (Fig. S4). As for the photocatalyst itself, it is well known that the photocatalytic activity is basically determined by efficiencies of three main steps such as light absorption, charge separation and surface catalysis [36,37]. The similar cocatalyst loading on the photocatalyst is expected to have the same surface catalysis, and the heterostructured sample BMTON/

Ta_3N_5(0.4) does not exhibit the widest visible light absorption compared to its counterparts BMTON and Ta_3N_5 (Fig. 1b). Accordingly, the significantly enhanced photocatalytic performance of the heterostructure can be reasonably ascribed to the promotion of charge separation and transfer ability.

In order to get insights into the possible promotion effect of the heterostructure on the charge separation, the Mott-Schottky (M–S) measurement, electrochemical impedance spectroscopy (EIS) analysis and time resolved infrared spectroscopy (TR-IR) measurement on the typical samples (BMTON/Ta_3N_5(0.4), BMTON and Ta_3N_5) were thus carried out. As seen in Fig. 4a, the M–S curve of BMTON/Ta_3N_5(0.4) exhibits a much smaller slop with respect to the single phase BMTON or Ta_3N_5, suggesting its much larger donor concentration according to the M–S equation [38]:

$$\frac{1}{C^2} = \frac{2}{\varepsilon \varepsilon_0 A^2 e N_D}(V - V_{fb} - \frac{k_B T}{e})$$

where C and A are the interfacial capacitance and area, respectively, V is the electrical bias applied, V_{fb} is the flat potential, k_B is Boltzmann's constant, N_D is the donor concentration, T is the absolute temperature, ε is the dielectric constant, and e is the electronic charge. Therefore, a plot of $1/C^2$ against V should yield a straight line from which V_{fb} can be determined from the intercept on the V axis. The value of N_D can also be conveniently compared due to its inverse proportion to the slope of the M–S curve. Namely, the smaller slop of M–S curves, the larger amount of donor concentration. On the basis of increased N_D observation, we can reasonably deduce that more photo-generated carriers can be produced upon light irradiation, indicating the possibility of heterostructure in enhancing spatial charge separation. A smaller charge transfer resistance and faster interfacial charge transport in the heterostructured sample can be further revealed by the EIS results given in Fig. 7a, where the much smaller radius of semicircular arc on the heterostructured sample can be observed with respect to the corresponding counterparts [39]. It should be pointed out that the radius of the arc in the EIS spectra can be generally used to judge the charge transfer resistance of the photocatalyst, and the smaller semicircular arc means much smaller resistance as well as faster charge transfer ability [40]. Another proof on the promotion of charge separation ability lies in the observation of the prolonged lifetime of carriers on the optimal heterostructured sample with respect to the single phase of BMTON or Ta_3N_5 (Fig. 7b) [21,27]. It is worth noting that the one-pot nitridation strategy for fabrication of heterostructure not only overcomes the thermal instability of nitrogen-doped oxide in air, but also makes a strong interaction at the interface contact. Both of them should be integrally responsible for the remarkably enhanced lifetime of carriers and the improved photocatalytic performance.

4. Conclusion

In summary, a series of heterostructured samples BMTON/Ta_3N_5(n) (n = 0-0.5) have been successfully synthesized by a simple one-pot nitridation route under the ammonia flow at 1223 K. To our knowledge, this should be the first fabrication of heterostructures containing complex perovskite with five elements (BMTON) by the one-pot nitridation strategy. Benefitting from the protection of ammonia flow and high temperature route, the structure of nitrogen-doped oxide BMTON can be well formed and maintained during the one-pot nitridation process, accompanying with formation of intimate interface with Ta_3N_5 for significantly enhanced charge separation as well as photocatalytic performances. As a result, it finally renders the nitrogen-doped BMTON sample to be feasibly used for construction of OWS system to achieve effective solar-to-chemical energy conversion. Our work not only highlights the importance of promotion of charge separation in fabricating OWS system, but also demonstrates the good generality of the one-pot nitridation route in fabricating more efficient nitrogen-doped oxide containing heterostructure systems for solar energy conversion.
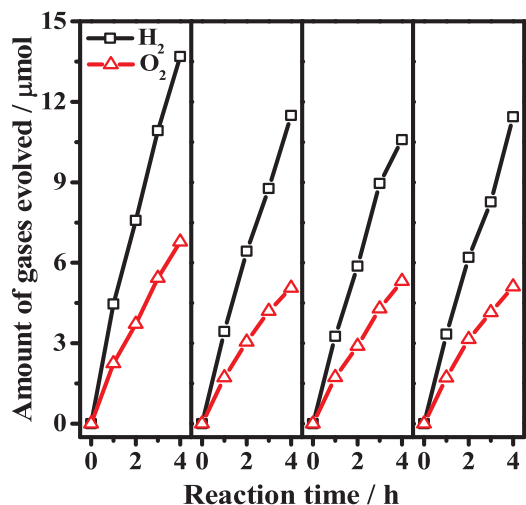

Fig. 6. Multiple cycles of time course curves about the Z-scheme OWS over the optimal heterostructured sample BMTON/Ta_3N_5(0.4).
Reaction conditions: 50 mg 0.5 wt% Pt-BMTON/Ta_3N_5(0.4), 100 mg 0.45 wt% PtO_x-WO_3, 100 ml aqueous NaI solution (0.8 mM), Pyrex top-irradiation type, 300 W xenon lamp.
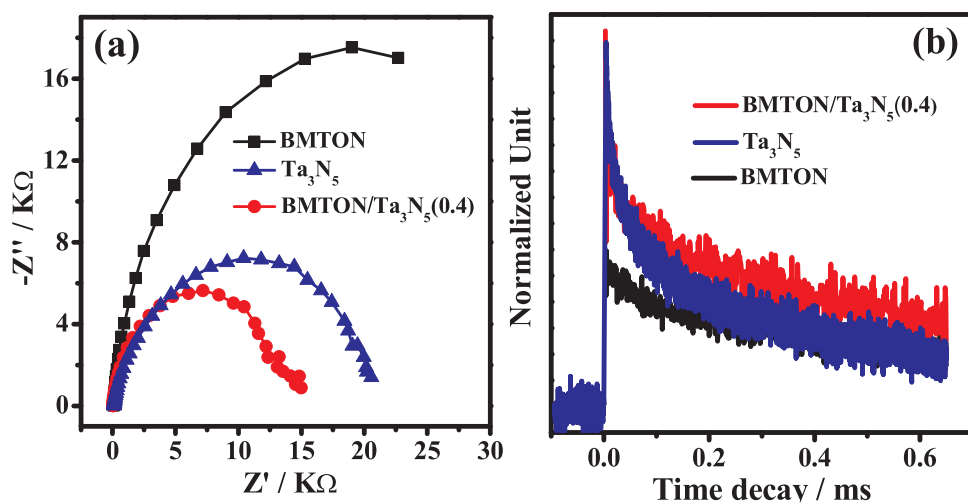
Fig. 7. (a) Nyquist plots of BMTON, BMTON/$Ta_3N_5(0.4)$ and Ta_3N_5 electrodes in 0.1 M Na_2SO_4 + 0.1 M NaI aqueous solution (pH = 9) under solar irradiation (AM 1.5 G); the sample electrodes are tested at 1.23 V vs. RHE; frequency: 0.1 Hz ~ 100 kHz. (b) Normalized transient absorption profiles of the representative samples loaded with Pt. The pulse laser at 355 nm was used to excite the samples for the IR tests. The cocatalyst of Pt with a loading amount of 0.5 wt% was deposited by impregnation and subsequent H_2 reduction method.

Appendix A. Supplementary data

Supplementary material related to this article can be found, in the online version, at doi:https://doi.org/10.1016/j.apcatb.2018.09.014.

References

[1] J.M. Bockris, Int. J. Hydrogen Energy 27 (2002) 731–740.
[2] J. Ogden, Prospects for Large-scale Use of Hydrogen in Our Future Energy System, Testimony to the Committee on Science, United States House of Representatives, Washington, DC, 2003.
[3] X. Chen, S. Shen, L. Guo, S.S. Mao, Chem. Rev. 110 (2010) 6503–6570.
[4] S. Chen, T. Takata, K. Domen, Nat. Rev. Mater. 2 (2017) 17050.
[5] K. Maeda, K. Domen, J. Phys. Chem. C 111 (2007) 7851–7861.
[6] H. Fujito, H. Kunioku, D. Kato, H. Suzuki, M. Higashi, H. Kageyama, R. Abe, J. Am. Chem. Soc. 138 (2016) 2082–2085.
[7] G. Ma, S. Chen, Y. Kuang, S. Akiyama, T. Hisatomi, M. Nakabayashi, N. Shibata, M. Katayama, T. Minegishi, K. Domen, J. Phys. Chem. Lett. 7 (2016) 3892–3896.
[8] R. Kuriki, T. Ichibha, K. Hongo, D. Lu, R. Maezono, H. Kageyama, O. Ishitani, K. Oka, K. Maeda, J. Am. Chem. Soc. 140 (2018) 6648–6655.
[9] T. Takayama, I. Tsuji, N. Aono, M. Harada, T. Okuda, A. Iwase, H. Kato, A. Kudo, Chem. Lett. 46 (2017) 616–619.
[10] R. Asahi, T. Morikawa, T. Ohwaki, K. Aoki, Y. Taga, Science 293 (2001) 269–271.
[11] R. Marschall, L. Wang, Catal. Today 225 (2014) 111–135.
[12] S. Chen, J. Yang, C. Ding, R. Li, S. Jin, D. Wang, H. Han, F. Zhang, C. Li, J. Mater. Chem. A 1 (2013) 5651–5659.
[13] X. Zong, G. Lu, L. Wang, Environmental Photochemistry Part III, Springer, Berlin, Heidelberg, 2013, pp. 87–113.
[14] A. Mukherji, R. Marschall, A. Tanksale, C. Sun, S.C. Smith, G.Q. Lu, L. Wang, Adv. Funct. Mater. 21 (2011) 126–132.
[15] C. Hu, H. Huang, Y. Huang, J. Energy Chem. 26 (2017) 515–521.
[16] K. Maeda, ACS Catal. 3 (2013) 1486–1503.
[17] J. Cui, T. Liu, Y. Qi, D. Zhao, M. Jia, G. Liu, F. Zhang, C. Li, J. Mater. Chem. A 5.35 (2017) 18870–18877.
[18] H. Wang, L. Zhang, Z. Chen, J. Hu, S. Li, Z. Wang, J. Liu, X. Wang, Chem. Soc. Rev. 43 (2014) 5234–5244.
[19] O. Ruzimuradov, M. Hojamberdiev, C. Fasel, R. Riedel, J. Alloys. Compd. 699 (2017) 144–150.
[20] M. Xie, X. Fu, L. Jing, P. Luan, Y. Feng, H. Fu, Adv. Energy Mater. 4 (2014) 1300995.
[21] S. Chen, Y. Qi, T. Hisatomi, Q. Ding, T. Asai, Z. Li, S.S.K. Ma, F. Zhang, K. Domen, C. Li, Angew. Chem. Int. Ed. 54 (2015) 8498–8501.
[22] Y. Qi, S. Chen, M. Li, Q. Ding, Z. Li, J. Cui, B. Dong, F. Zhang, C. Li, Chem. Sci. 8 (2017) 437–443.
[23] M. Christian, C. Philippe, D. Bernard, J. Am. Ceram. Soc. 53 (1970) 56–57.
[24] G. Hitoki, A. Ishikawa, T. Takata, J. Kondo, M. Hara, K. Domen, Chem. Lett. 31 (2002) 736–737.
[25] S. Janaswamy, G. Sreenivasa Murthy, E.D. Dias, V.R.K. Murthy, Mater. Lett. 55 (2002) 414–419.
[26] Y. Lee, H. Teng, C. Hu, S. Hu, Electrochem. Solid-State Lett. 11 (2008) 1–4.
[27] S. Chen, S. Shen, G. Liu, Y. Qi, F. Zhang, C. Li, Angew. Chem. Int. Ed. 54 (2015) 3047–3051.
[28] K. Gelderman, L. Lee, S.W. Donne, J. Chem. Educ. 84 (2007) 685.
[29] B. Ohtani, K. Iwai, Si. Nishimoto, S. Sato, J. Phys. Chem. B 101 (1997) 3349–3359.
[30] Y. Miseki, S. Fujiyoshi, T. Gunji, K. Sayama, Catal. Sci. Technol. 3 (2013) 1750–1756.
[31] H. Suzuki, O. Tomita, M. Higashi, R. Abe, Catal. Sci. Technol. 5 (2015) 2640–2648.
[32] R. Abe, M. Higashi, K. Domen, ChemSusChem 4 (2011) 154.
[33] K. Maeda, M. Higashi, D. Lu, R. Abe, K. Domen, J. Am. Chem. Soc. 132 (2010) 5858–5868.
[34] A. Ryu, Bull. Chem. Soc. Jpn. 84 (2011) 1000–1030.
[35] Y. Miseki, S. Fujiyoshi, T. Gunji, K. Sayama, Catal. Sci. Technol. 3 (2013) 1750.
[36] Q. Wang, T. Hisatomi, Q. Jia, H. Tokudome, M. Zhong, C. Wang, Z. Pan, T. Takata, M. Nakabayashi, N. Shibata, Y. Li, I.D. Sharp, A. Kudo, T. Yamada, K. Domen, Nat. Mater. 15 (2016) 611.
[37] T. Takata, C. Pan, K. Domen, Sci. Technol. Adv. Mater. 16 (2016) 033506.
[38] F. Cardon, W.P. Gomes, J. Phys. D 11 (1978) L63.
[39] Q. Wang, J.E. Moser, M. Grätzel, J. Phys. Chem. B 109 (2005) 14945–14953.
[40] A. Fujishima, X. Zhang, D.A. Tryk, Surf. Sci. Rep. 63 (2008) 515–582.